Optical Engineering 45(11), 115001 (November 2006)

Total column oxygen detection using a Fabry-Perot interferometer

Elena Georgieva, MEMBER SPIE
Science Systems and Applications, Inc.
Lanham, Maryland 20706
E-mail: egeorgie@pop500.gsfc.nasa.gov

Emily Wilson
NASA Goddard Space Flight Center
Code 554
Greenbelt, Maryland 20771

M. Miodek
Science Systems and Applications, Inc.
Lanham, Maryland 20706

William S. Heaps
NASA Goddard Space Flight Center
Code 554
Greenbelt, Maryland 20771

Abstract. A passive instrument based on a Fabry-Perot interferometer was designed and used for oxygen atmospheric column absorption measurements. The instrument operates in the oxygen A-band spectral region from 759 to 771 nm. Surface solar irradiation reflected off the Earth is detected using two channels at two wavelengths—one for pressure sensing and the other for temperature sensing. Each channel of the O_2 column measurement system consists of two subchannels—Fabry-Perot and reference. Solid Fabry-Perot etalons were designed and used to confine the response to the O_2 absorption bands. The etalons have free spectral ranges of 0.575, 0.802, and 2.212 nm. Two narrow bandpass filters (760 to 764 and 767 to 771 nm) were also used. The instrument is sensitive to changes in oxygen column as small as 0.88 mbar for ground-based experiments and 5 mbar for airborne measurements. The major advantages of the optical setup are its compactness, high sensitivity, high signal-to-noise ratio, and stability for both ground and airborne experiments.
[DOI: 10.1117/1.2387878]

Subject terms: Instrumentation, measurement, and metrology; remote sensing; atmospheric composition; optical instruments; absorption; interferometry; Fabry-Perot.

Paper 050707R received Sep. 2, 2005; revised manuscript received Mar. 29, 2006; accepted for publication Apr. 24, 2006; published online Nov. 14, 2006. This paper is a revision of a paper presented at the SPIE conference on Earth Observing Systems IX, Aug. 2004, Denver, Colorado. The paper presented there appears (unrefereed) in SPIE Proceedings Vol. 5542.

1 Introduction

Precise measurements of trace gas concentrations are important for understanding the physical processes in the atmosphere and hence for prediction of climate changes and better understanding of global warming.

Remote sensing of the atmosphere using the oxygen A band has been studied for many years. Different techniques, both active and passive, were used to determine the cloud-top pressure and temperature. The Profiling A-Band Spectrometer Visible Imager (PABSI) measured the atmospheric radiance of the O_2 A band and determined the optical depth and altitude of thin clouds and aerosols. Retrievals of aerosol and cloud properties were done by Stephens and Heidinger.[1–3] The Global Ozone Mapping Experiment (GOME) onboard the ERS-2 satellite measured the oxygen A band to obtain information on the altitude distribution of aerosols.[4] SCIAMACHY[5] (Scanning Imaging Absorption Spectrometer for Atmospheric Chartography) was designed to measure atmospheric trace gases such as O_3, NO_2, O_2, $(O_2)_2$, and H_2O. MERIS[6,7] (Medium Resolution Imaging Spectrometer) is measuring the solar radiation at the top of the atmosphere, where sun radiation is attenuated mainly because of O_2 absorption, and gives information about the surface elevation.

O'Brien et al.[8] measured the surface pressure from a research aircraft, using the oxygen A band of sunlight reflected from the sea surface and a grating spectrograph directed toward the sun. They showed that the scattering cannot be neglected and the scattered radiance depends primarily on the adjusted airmass. The accuracy of their instrument was 2 kPa (20 mbar), and after the analysis they derived additional information about the scattered radiance and enhanced the accuracy to 1 mbar. O'Brien and Mitchell[9] also studied the temperature sensitivity of the A-band absorption.

Stam et al.[10] numerically studied cloud top altitudes from reflected sunlight radiances in the A band. Their conclusion is that the polarization of the reflected light should be measured with the same spectral resolution as the radiances to minimize the errors due to instrument polarization sensitivity. The authors also performed radiative transfer calculations for a theoretical investigation of the behavior of the linear polarization of the light emerging from the top of the cloudless atmosphere in the wavelength region of the O_2 A absorption band. The degree of linear polarization was determined using the Stokes vector calculus and four model atmospheres; the result of their work was that for a given surface albedo, the variation of polarization across an absorption line depends on the scattering properties of the atmospheric particles and on their vertical distribution. In an inhomogeneous atmosphere, in which the scattering properties vary with the altitude, the degree of linear polarization of reflected light outside an absorption line can dif-

0091-3286/2006/$22.00

fer significantly from that inside a line; that is a problem for polarization-sensitive spectrometers like GOME and SCIAMACHY.

Cloud altitude determination using the oxygen A band was studied by Wark and Mercer,[11] Saiedy et al.[12] and Kuze and Chance.[13] The last of these expected that a proper combination of the satellite radiance measurements and cloud scattering models would suffice to separate albedo and cloud reflectivity and to obtain high accuracy. The authors determined the cloud top height and cloud coverage parameter by least-squares fitting to calculated radiance ratios in the oxygen bands.

Fisher and Grassl[14] also did radiative transfer calculations to derive the cloud-top pressures, from backscattered solar radiances, using oxygen A-band absorption. Cloud properties like the cloud-top height, optical thickness, droplet size distribution, and temperature need to be included in calculations so that more precise climate study can be achieved. Fisher et al.[15] used a lidar technique and did radiance measurements with an optical multichannel analyzer so as to compare the calculated and measured radiances. They investigated low-level stratus clouds using the absorption in the oxygen A band and found that the physical processes within and at the upper layer of the cloud are different. The cloud-top heights predicted by their algorithm agree well and are close to the results of Boers et al.[16]

Breon and Bouffies[17] achieved land surface pressure estimates with the POLDER (Polarization and Directionality of the Earth Reflectance) instrument, which covered the oxygen A band. The authors developed a radiative transfer model that connected single scattering with the surface reflectance. The validity of the model decreases with increasing aerosol optical thickness when multiple scattering occurs.

Most recently, Daniel et al.[18] studied the absorption by oxygen along with the O_2-O_2 collision complex and oxygen B band in order to retrieve better information about cloud parameters. In addition to O_2 discrete lines, there is broadening from the O_2-O_2 collision complexes. Retrieving data from the oxygen B band (686 to 698 nm) along with O_2-O_2 collision absorption (477 nm) in addition to retrieving data from the oxygen A band (755 to 775 nm) decreases the uncertainty in retrieving the cloud parameters by more than 50% compared to using the oxygen A band alone. Their retrieval did not require calibrated radiance measurements.

The dayglow, absorption, and emission of the O_2 atmospheric bands were studied in a number of papers.[19–21] The authors present theoretical models and experimental results with a Fabry-Perot interferometer flying on Dynamics Explorer 2 to investigate the brightness of the emission of the A band in the thermosphere, and their instrument allowed the daytime emission to be observed between 60 and 300 km.

There has been a lot of research done using the oxygen A band and different spectroscopic techniques, active and passive. The passive instruments can be more easily deployed on an aircraft or a satellite. The active techniques using lidar methods need to operate stable laser systems in space and thus are technically more difficult. The prototype Fabry-Perot instrument that we constructed is passive, has high sensitivity and reduced dimensions in comparison with other instruments, and has already gone through rigorous laboratory, ground-based, and airborne experiments. The initial results show that the instrument is particularly sensitive and with ground measurements we can detect changes as small as 0.88 mbar in 1 s; the airborne sensitivity is 5 mbar in 0.1 s at present.

The purpose of this paper is to demonstrate the architecture, design, and testing (laboratory, ground-based, and airborne) of a new remote sensing instrument using a novel technique. The performance specifications of the instrument and its peculiarities are described in detail. The concept of the instrument and the technology can be used to target other trace species as well.

2 Measurement Approach

The instrument is based on a novel application of a Fabry-Perot interferometer and was constructed and assembled at NASA's Goddard Space Flight Center under the Instrument Incubator Program. Laboratory and ground-based tests were performed to evaluate the system's performance. An improved version of the instrument was recently deployed and tested at Dryden Flight Research Center aboard NASA's DC-8 Airborne Science Laboratory.

The instrument was designed to have two channels—an oxygen-pressure-sensing channel to take account of the pressure variations, and an oxygen-temperature-sensing channel. The purpose of the latter is not to measure the geophysical temperature but to correct the pressure channel data. The pressure channel is well defined by a narrow bandpass filter, which selects a spectral range from 760 to 764 nm of the oxygen A band, where the absorption coefficient is less sensitive to temperature. The temperature-sensing channel uses a different bandpass filter (767 to 771 nm), where the oxygen absorption lines are more sensitive to temperature changes. The narrow bandpass filters have 30-mm clear aperture.

Each of the two channels of the measurement system consists of two subchannels—the subchannel that includes the Fabry-Perot etalon, hereafter called the Fabry-Perot subchannel, and the reference subchannel,[22,23] which detects the total light intensity limited by the bandpass filter's spectral range. We used solid fused silica Fabry-Perot etalons with clear aperture of 30 mm and with highly reflective coatings on both surfaces. The light that passes through the etalon undergoes multiple reflections on each inside surface, creating an interference pattern of equidistant fringes that depends on the frequency. The width of the passbands depends on the quality of the coatings and on the flatness and parallelism of the surfaces. The Fresnel formalism gives the reflected and transmitted amplitude components for the light wave as functions of the optical constants of the two media and the angle of incidence. The resulting intensity follows the Airy function distribution pattern. An ideal Fabry-Perot etalon with perfectly flat surfaces transmits a narrow spectral band, and the energy transmission coefficient I_T is given by[24]

$$I_T = \frac{T^2}{(1-R)^2}\left[1 + \frac{4R}{(1-R)^2}\sin^2\left(\frac{2\pi nd\cos\theta}{\lambda}\right)\right]^{-1}, \qquad (1)$$

where λ is the wavelength, n is the refractive index, d is the thickness of the etalon, θ is the angle of incidence within

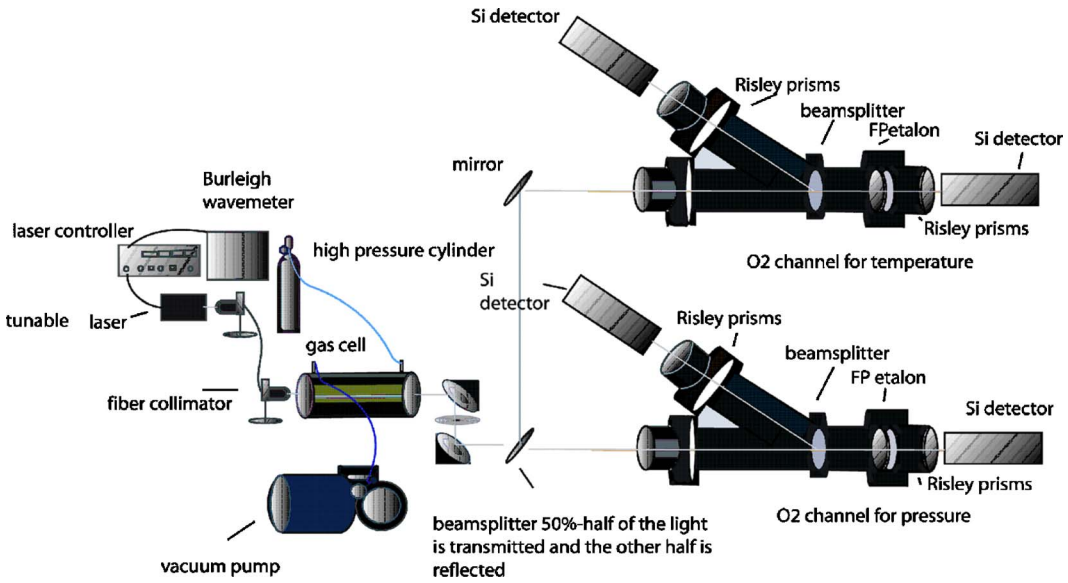

Fig. 1 The laboratory version of the O_2 measurement system.

the cavity, T is the intensity transmission coefficient for each coating, and R is the intensity reflection coefficient. The most important parameters of the etalon are the free spectral range (FSR), which is the spacing between the passbands; the reflection finesse N_R, which depends only on the reflectivity of the coatings; and the contrast C, defined as the ratio of the transmission at the maximum of the passband to the transmission at the minimum between the fringes. The FSR is given by[24,25]

$$\mathrm{FSR} = \frac{\lambda^2}{2nd\cos\theta}, \tag{2}$$

the reflection finesse is

$$N_R = \frac{\pi R^{1/2}}{1-R}, \tag{3}$$

and the contrast is

$$C = \left(\frac{1+R}{1-R}\right)^2. \tag{4}$$

Three different solid Fabry-Perot etalons with FSRs of 0.575, 0.802, and 2.212 nm and refractive index $n = 1.4538$ at $\lambda = 762$ nm were used. The thickness of the etalon should be accurately calculated in advance so the transmitted fringes can be aligned with the O_2 absorption lines. The solid Fabry-Perot etalons have a fixed passband and can be coarse-tuned by tilting. In order to fine-tune the etalons' transmission lines we used the strong temperature dependence of the refractive index of fused silica. The spectral shift is due to the change of the refractive index of the etalon's optical material. It depends on the temperature as

$$n = n_0 + \beta(T - T_0), \tag{5}$$

where n_0 is the refractive index at temperature T_0, and β is the thermal coefficient of the refractive index of the fused silica, $\beta = 1.28 \times 10^{-5}$ K^{-1}. The transmission lines shift to longer wavelengths by typically 0.02 nm/K for fused silica.[26] The temperature was varied in steps of 0.01 K, as we wanted to fully explore the etalons' performance. The controllers' stability by specification is <0.002 K. The temperature sensors' precision is <0.01 K. The temperature needs to be controlled with 0.5-K precision to keep the alignment stable. The stability of the temperature is important because even small temperature instability during the experiment can cause variations in the wavelength of transmitted fringes.

3 Experimental

3.1 *Instrument Setup*

The instrument setup is shown in Fig. 1. The incoming light is collimated by two off-axis parabolic aluminum mirrors. The field of view is limited by a 2-mm pinhole positioned at the focal point of the mirrors. A chopper was used to modulate the light at 380 Hz. The incoming light is then split between the pressure- and temperature-sensing channels by a 50-50 beamsplitter. The two channels are identical except for the wavelengths. The first one was designed for measurements of the pressure variations, and the second one for temperature variations of the atmospheric oxygen column. The incoming light was first prefiltered at a central wavelength of 762 nm and directed through the pressure-sensing channel. The prefilter was mounted in a temperature-controlled oven to avoid wavelength fluctuations. The windows of the oven were wedged to avoid internal interference. The light is then split between the Fabry-Perot and reference subchannels of the pressure-sensing channel, with 90% of the light going to the Fabry-Perot subchannel. In the Fabry-Perot subchannel the light

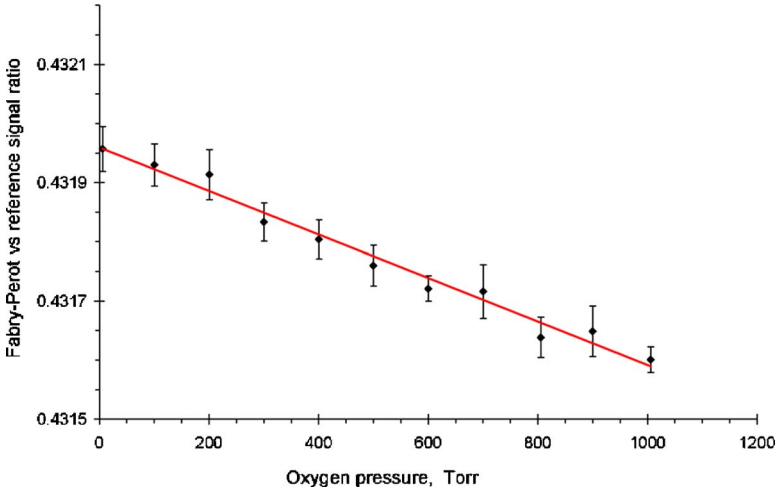

Fig. 2 Pressure-sensing channel: the ratio as a function of oxygen pressure. Experimental points with error bars, and linear fit.

passes through the Fabry-Perot etalon mounted in a temperature-controlled oven for fine FSR tuning. The windows of the oven are again wedged to avoid internal interference. A set of Risley prisms directs the beam to be focused on a Si detector mounted at the focal plane of the focusing lens. The temperature-cooled detectors' sensitivity is 150 V W^{-1}. Both Fabry-Perot and reference signals were measured using the lock-in amplifier technique.

Our measurement setup uses four lock-in amplifiers (model SR830 from Stanford Research Systems). Custom LabVIEW-based software has been developed for controlling the measurement system and collecting the data. The independent parameters set at the beginning of the measurement series were the temperatures of the bandpass filters and the solid Fabry-Perot etalons, the time constants for the lock-in amplifiers, and the sampling frequency. They were monitored constantly. A warm-up time of 20 min was provided. We monitored also the temperature controllers, the temperature of the instrument box, and the ratio of the Fabry-Perot subchannel to the reference subchannel intensity of both temperature- and pressure-sensing channels. The data were collected with time constant 0.1 s and analyzed using IDL routines to handle large data sets and plot experimental data as signal ratios and airmasses. The IDL routines were also used to model the expected performance of each hardware version of the instrument, based on the following independent parameters: refractive index of fused silica, temperature of the atmosphere, oxygen molecule data from Hawks (HITRAN atmospheric software), observed ground area, albedo, altitude, detector efficiency, prefilter peak transmission, spectral range of interest, and finesse of the solid Fabry-Perot etalon.

3.2 *Laboratory Measurements*

The experimental setup as discussed is shown in Fig. 1. A tunable laser coupled to a multimode fiber was used as a light source. The light exiting the fiber was collimated and directed to a gas cell. The gas cell used in this experiment is 1.5 m long. Two different etalons were used in the Fabry-Perot subchannel module of the pressure-sensing channel. The first one has an FSR of 0.802 nm, and the second of 2.212 nm. For the temperature-sensing channel we used a different multipass gas cell with 80-m effective path length, and we also used a third etalon (FSR 0.575 nm) for a Fabry-Perot subchannel module. The light exiting the gas cell was collimated and directed to the instrument temperature- and pressure-sensing channels.

3.2.1 *The pressure-sensing channel*

Measurements with the FSR=0.802-nm *etalon, active Fabry-Perot subchannel.* The first measurement approach was to detect the oxygen absorption using the change of the intensity in the Fabry-Perot subchannel. We achieved that through aligning the Fabry-Perot etalon transmission lines with the strong oxygen absorption lines in the P branch of the oxygen A band using fine temperature tuning of the etalon. The corresponding thickness of the etalon is 0.249 mm. We recorded laser scans from 760 to 764 nm, in increments of 0.006 nm, of the gas cell filled with pure oxygen at 500-Torr pressure at room temperature. The Fabry-Perot etalon was mounted in an oven heated to 20°C. The Fabry-Perot subchannel is very sensitive to the pressure in the gas cell. The transmittance of the Fabry-Perot etalon decreases with increasing pressure. The ratio of the transmitted intensity of the Fabry-Perot to that of the reference subchannels, hereafter called simply the *ratio*, decreases with increasing gas pressure. A pressure of 1000 Torr yields a column absorption equal to 0.1% of the atmospheric column. The response of the ratio to the pressure change is shown in Fig. 2. The pressure change from 0 to 1000 Torr causes a decrease in the ratio. Both experimental points with error bars and the trend line are shown in this figure.

Measurements with the FSR=2.212 nm *etalon, active reference subchannel, active measurement.* Our second approach to measuring the oxygen absorption is based on the change in the reference subchannel intensity while

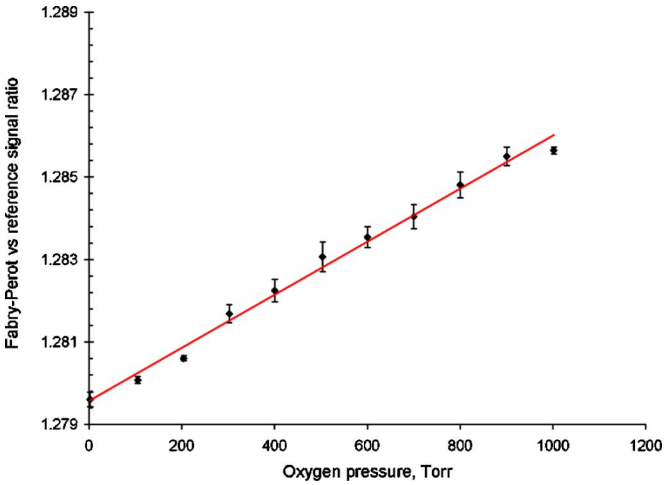

Fig. 3 Pressure-sensing channel: the ratio as a function of oxygen pressure. Experimental points with error bars, and linear fit. The Fabry-Perot transmission line is placed in the gap between the absorption lines of the oxygen A band.

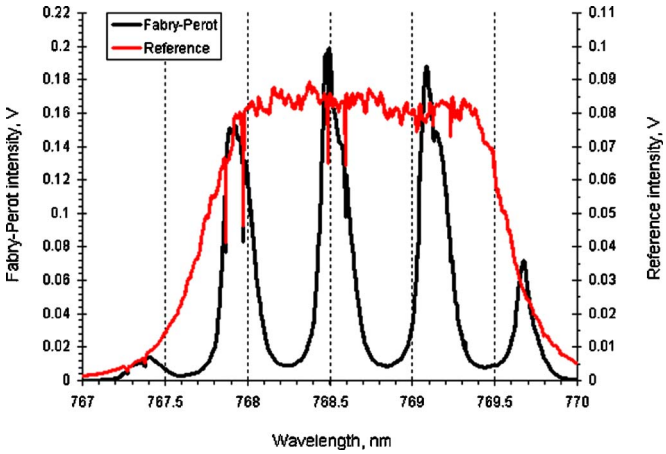

Fig. 4 Temperature-sensing channel: experimental fine-tuning. The Fabry-Perot transmission lines are aligned with the oxygen absorption bands.

using the Fabry-Perot intensity as a base value. We designed a new Fabry-Perot etalon with FSR 2.212 nm for this measurement. This etalon has only one transmission line in the bandpass filter spectral range of 760 to 764 nm. Fine temperature tuning of the etalon was used to place the transmission line in the gap between the P and R branches of the oxygen A band. In this way all oxygen absorption doublets are blocked by the Fabry-Perot etalon. They are, however, detected by the reference subchannel, making it the active channel for this experiment.

The advantages of this setup are better sensitivity, better repeatability, easier temperature alignment of the Fabry-Perot etalon, and less noise. The ratio of Fabry-Perot to reference subchannel intensity becomes more sensitive to pressure changes in the gas cell.

The ratio as a function of the oxygen pressure in the gas cell is presented in Fig. 3. Here again the experimental points are shown with error bars and the trend line is included. Our scans show that at 22°C temperature of the Fabry-Perot etalon, its transmission line can be placed exactly in the gap between the two branches of the oxygen A band.

3.2.2 *The temperature-sensing channel*

We used the active measurement approach as described in connection with the pressure-sensing channel (Sec. 3.2.1). The spectral region between 767 and 770 nm was chosen because the oxygen absorption lines are very sensitive to the temperature changes there, the absorption lines are very well defined, and we were able to easily align the Fabry-Perot transmission lines to the oxygen lines and to keep the alignment stable for extended periods of time. We used a Fabry-Perot etalon with FSR 0.575 nm, corresponding to thickness 0.355 mm, and were able to align it with oxygen absorption lines by increasing the temperature of the etalon to 71°C (Fig. 4). The multipass gas cell with path length 80 m was used at this experiment. The gas pressure in the cell was 350 Torr, and the temperature was 22°C. The temperature channel was used to obtain the weighted-average atmospheric column temperature for use with the data on the pressure-sensing-channel.

3.3 *Ground-Based Measurements*

The Earth's surface is usually treated as Lambertian (the reflected radiation is assumed to be unpolarized and isotropic) for space- and airborne remote sensing applications. However, natural surfaces are usually non Lambertian: they scatter anisotropically and can be characterized by their bidirectional reflection distribution function. The solar flux becomes polarized to some degree in passing through the Earth's atmosphere and is diffusely reflected from trees, grass, etc. The light illuminating a region on the surface consists of a specular and a scattered component. The strength of the scattered component depends on the atmospheric conditions and the nature of the scatterers. A cloudy sky performs as a good diffuser of the passing radiation, so the incident light is fully diffused on cloudy days. For a clear sky in Greenbelt, MD, the measured direct component is approximately 80% of the total incident solar radiation in the visible and infrared regions.

Using basically the same setup as shown in Fig. 1, we performed a series of ground-based O_2 atmospheric column absorption measurements. The presented results are of a ground-based experiment performed in Greenbelt, MD under cloudy atmospheric conditions. The diffusely scattered light behaves differently from the specular, which affects the total O_2 column absorption. The net effect is difficult to quantify because of the wavelength-dependent properties of the cloud particles and the fact that the scattering particles are different and may change rapidly. The atmospheric backscattering, for example, will decrease the total column absorption. The measurements were performed with the instrument looking at a Spectralon spectrally flat diffuse reflective target. The scattered light was directed into the instrument with the mirror mounted at 45 deg. The instrument was placed in a temperature-controlled box to protect it from environmental perturbations. The path length of the light through the atmosphere has a scattered

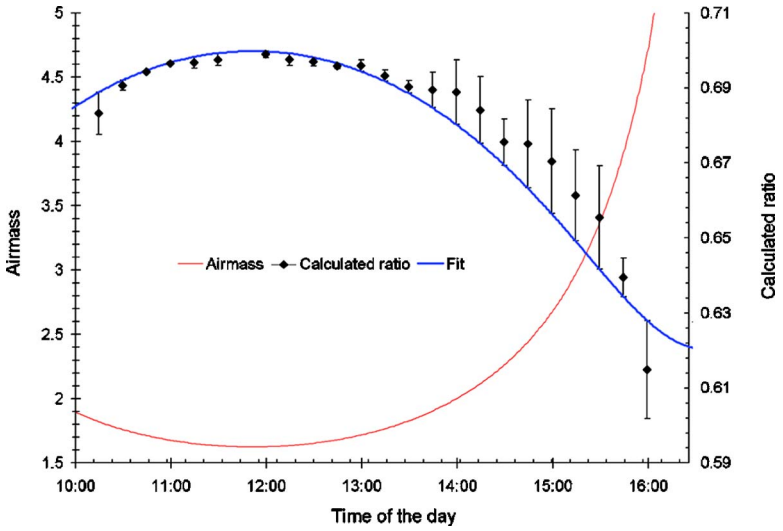

Fig. 5 Calculated ratio for field measurements: prefilter at 762 nm, Fabry-Perot etalon temperature 20°C. The measurement was performed with the instrument looking at the Spectralon target. Local daylight saving time is used.

component introduced by scattering of various aerosols. The scattered component can profoundly affect the path length of the light through the atmosphere. We attempted to eliminate it by blocking the direct beam at regular intervals and using the data taken with the blocked beam to correct for the scattering. We express the dependence of the two signals at blocking by the *calculated ratio*

$$R_{\text{cal}} = \frac{I_{\text{FP1}} - I_{\text{FP2}}}{I_{\text{Re1}} - I_{\text{Re2}}}, \tag{6}$$

where I_{FP1} is the intensity in the Fabry-Perot subchannel when the Spectralon target is not blocked and the light has both specular and diffuse components, and I_{FP2} is the intensity in the Fabry-Perot subchannel when the specular beam is blocked and only diffuse light is entering the instrument. Similary, for the reference subchannel, I_{Re1} is the intensity when the Spectralon is unblocked, and I_{Re2} is the intensity when the specular beam is blocked. The calculated ratio R_{cal} is different from the ratio we used in previous subsection. Using this approach, we were able to obtain the R_{cal} of the Fabry-Perot subchannel intensity versus the reference subchannel intensity, which depends mostly on the specular component of incident solar radiation. This R_{cal} corresponds very well to the change of the airmass (the secant of the zenith angle) during the day. To allow for the sphericity of the earth in spite of the plane-parallel approximation, the Chapman function replaces the secant of the zenith angle. The airmass is an indication of the path length the solar radiation travels through the atmosphere. An airmass of 1.0 means the Sun is directly overhead and the radiation travels through one atmosphere thickness. The airmass describes the amount of atmosphere that solar radiation passes at a given time and changes during the day as the Sun moves in the sky. At low altitude angles the airmass is much larger (the solar radiation needs to pass a longer distance through the atmosphere) than when the Sun is near its zenith.

A Fabry-Perot etalon with FSR 0.802 nm and thickness 0.249 mm was used in the ground-based experiment performed in Greenbelt, MD. The separation between the transmission lines of this etalon matched the separation between the oxygen absorption lines in the P branch of the oxygen A band. The R_{cal} is inversely proportional to O_2 concentration and reflects the airmass change over time as shown in Fig. 5. Figure 6 shows how R_{cal} decreases with the increase of airmass during the day. The result confirms our conclusions from the lab measurements using the same etalon (Fig. 2).

A new ground-based experiment using a Fabry-Perot etalon with FSR 2.212 nm was performed at NASA's Dryden Flight Research Center, CA, in May 2004 under clear atmospheric conditions. A sun tracker was used for the measurements to keep the input optics always best oriented. Fiber optics directed the solar radiation into the instrument, avoiding stray light from close objects. The intensity ratio of the Fabry-Perot subchannel to the reference subchannel as a function of the airmass is presented in Fig. 7. The ratio increases with increasing airmass: a larger airmass means more oxygen, more absorption, and a smaller reference signal. We can see how well the ratio of the two signals and the airmass for the day are correlated. The standard atmospheric pressure equals 1013 mbar at sea level. The measured ratio of Fabry-Perot subchannel to reference subchannel intensity equals 0.00087 airmass units at 1-s integration time. Therefore the measured ratio noise is estimated to be 0.88 mbar. The precision demonstrates that the instrument has real potential for use as a ground sensor to correct for terrain variations of measurements of a trace species such as CO_2.[27,28] The same experiment was performed at a different day, again at Dryden, and the ratio of the two signals (Fabry-Perot to reference) was measured and is plotted with the airmass changes as a function of time in Fig. 8.

The temperature dependence on the ratio of Fabry-Perot to reference signal is presented in Fig. 9. The temperature-sensing channel was operated in the spectral region 767 to 771 nm, where the oxygen absorption lines are very sensitive to temperature changes. The ratio of the two signals

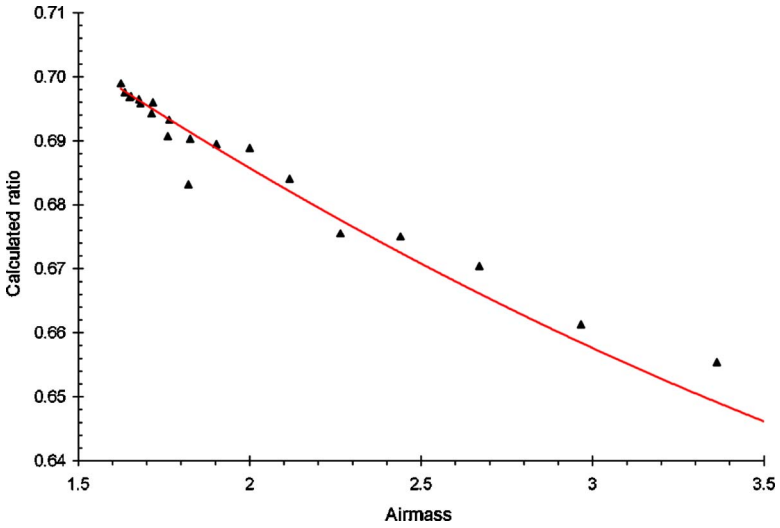

Fig. 6 The calculated ratio and trend line as a function of the airmass.

(Fabry-Perot/reference) decreases with increasing average atmospheric column temperature during the day.

3.4 *Airborne Measurements*

In order to prepare our instrument for airborne test measurements, we designed and built a flight-hardened version slightly different from the previous ones. The modifications were necessary because the flight version was exposed to more mechanical stress. The electronics were also ruggedized for operating onboard NASA's flight laboratory—a DC-8 aircraft. The two channels have reduced dimensions, and instead of lenses we used two gold-coated off-axis parabolic mirrors to focus the light onto the detectors. The flight unit also employs more rugged optical mounts and integrated optical shielding.

We measured the intensity of light reflected from the Earth's surface. The solar radiation passes through the atmosphere, reflects off the Earth's surface, and then enters the instrument through a downward-viewing mirror, which views the ground through a portal in the bottom of the DC-8 aircraft. The incident light is then collimated with the two off-axis parabolic mirrors. The pinhole diameter is 2 mm, and the instrument field of view is 20 mrad. The instrument was mounted on 12-mm-thick aluminum plate within a fiberglass enclosure through vibrationally isolated wire-rope mounts positioned at the bottom four corners of the enclosure.

The measured data of our first flight are shown in Fig. 10. The DC-8 was flying south over the San Joaquin valley of central California, and the aircraft slowly descended from 6150 to 300 m and then began to climb back up. The airplane altitude is plotted in gray, and the ratio of the Fabry-Perot signal to the reference signal for the pressure-sensing channel is the black line. The pressure in the atmosphere increases with decreasing altitude, dropping off almost exponentially at lower altitude. But percentage of oxygen (its mixing ratio) remains the same, 21% of the total air. When the airplane climbs up, the solar radiation

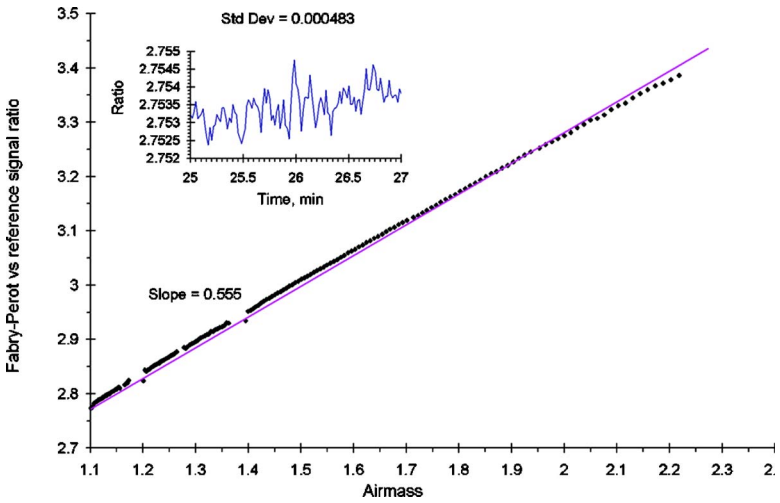

Fig. 7 Ratio as a function of the airmass: experimental points and linear fit. The inset graph shows an expaned plot of the measured ratio for 2 min; the given standard deviation is calculated.

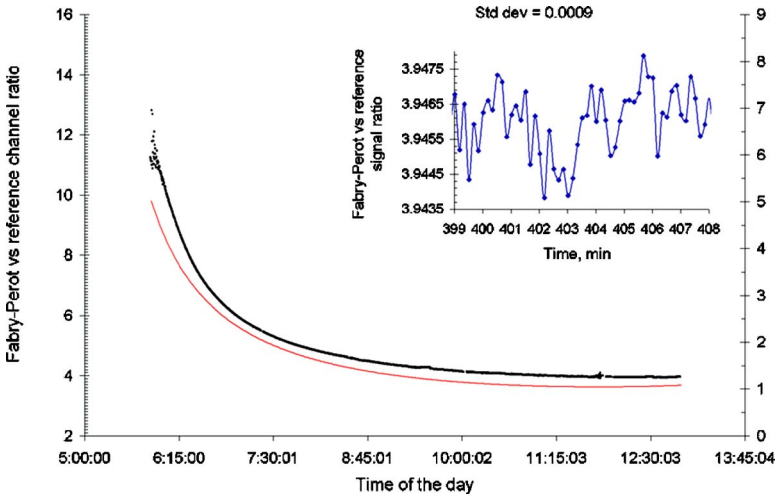

Fig. 8 The ratio (black line) and the airmass (gray line) against time. Local daylight saving time is used. The inset graph shows an expanded plot of the measured ratio for 9 min; the given standard deviation is calculated.

passes through more airmass and therefore more oxygen, and the ratio of the two signals increases (Fig. 10). The spikes in the ratio arise from data obtained when the aircraft was turning. As we see, the ratio is tracking very well the pressure altitude of the plane during the flight. During the first 20 min the ratio is not constant, because the Fabry-Perot etalon temperature is not stable yet. When the aircraft is going down, the path of the beam is shorter; that means less absorption, a bigger reference signal, and as a result a smaller ratio. The standard deviation is calculated to be 0.00393 (Fig. 10). The ratio of the two signals changes by about 0.8 per unit airmass. The noise in the ratio of Fabry-Perot to reference subchannel intensity in the pressure-sensing channel corresponds to 0.005 airmass units at 0.1-s integration time. We can detect changes in pressure as small as 5 mbar in 0.1 s in the airborne experiment.

The airmass changes were also calculated and are shown in Fig. 10. The aircraft radar altimeter and atmospheric pressure at corresponding altitude were used to derive the surface pressure, assuming a standard atmospheric profile. The airmass was calculated as the slant column from the sun at the top of the atmosphere to the surface plus the distance from the surface at nadir to the airplane.[28,29]

For the airborne pressure-sensing experiments the solid etalon with FSR 2.212 nm was used. The expected intensities for all subchannels of the instrument, their ratio, the standard deviation, and sensitivity were then calculated. The calculated ratio of the signals in the subchannels corresponds to our experimental data. The sensitivity calculated by the model is better than the sensitivity for the aircraft measurements. That is not a surprise, because in the real measurement the environment is not ideal, we have rapidly changing albedo, clouds, airplane vibrations, temperature, atmospheric turbidity, and precipitable water vapor. All those factors reduce the sensitivity in comparison with the modeled sensitivity.

The flight test data for the temperature-sensing channel are presented in Fig. 11. The flight was on 17 May, a

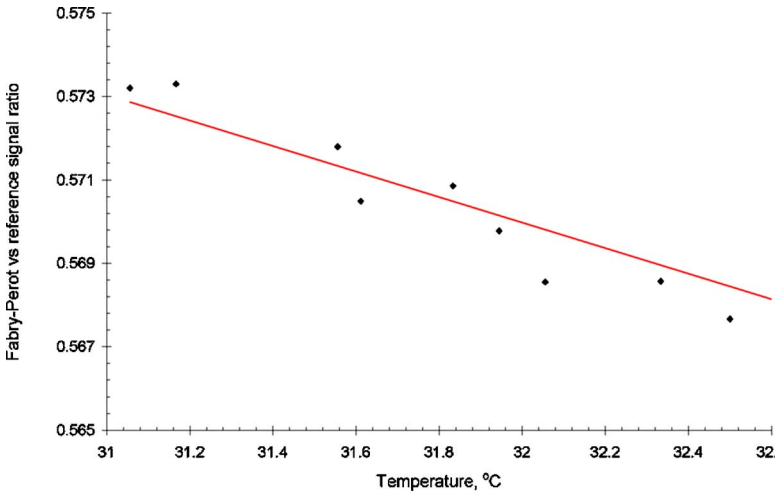

Fig. 9 Temperature-sensing channel: the ratio as a function of temperature. Experimental points and linear fit.

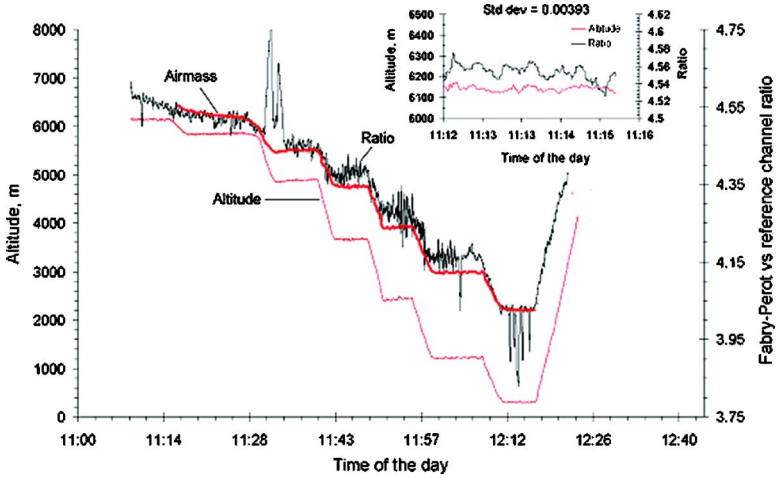

Fig. 10 The instrument's response to the altitude in meters on the airborne mission. The ratio for the pressure-sensing channel and the airmass as a function of time are shown. The inset graph shows expanded plots of the measured ratio and altitude for 4 min. The standard deviation is calculated to be 0.00393. Local daylight saving time is used.

cloudy day; the data for the temperature are from the information collection and transmission system (ICATS) of the DC-8 plane; they were saved and analyzed after the flight. When the average column temperature decreases, the ratio of Fabry-Perot to reference intensity increases. The dependence matches the changes detected in the lab with the gas cell using the same etalon. The oxygen absorption lines in the spectral region 767 to 769 nm become almost twice as strong on increasing the temperature from 260 to 310 K. The Fabry-Perot subchannel signal decreases as the oxygen absorption lines are aligned with the Fabry-Perot etalon transmission lines. Therefore the ratio of Fabry-Perot to reference intensity decreases as well. The aligning of the Fabry-Perot transmission lines with the oxygen absorption lines in lab measurements is shown in Fig. 4. Figure 9 shows ground-based measurements with the temperature-sensing channel, and Fig. 11 shows the flight data.

Conclusions

We have designed and tested an instrument, based on a Fabry-Perot etalon, for total atmospheric column measurements of the surface pressure in the oxygen A band. We have demonstrated the instrument's significant capability to detect O_2 in laboratory, ground-based, and airborne experiments. Our estimate of the system's performance indicates that with the current design and a sun tracker, the instrument's sensitivity to oxygen column changes is as good as 0.88 mbar in ground-based experiments. The precision shows that the instrument has real potential for use as a ground sensor to correct for terrain variations of measurements of a trace species such as CO_2. To be useful for this purpose, the precision of the O_2 measurement needs to be somewhat better than 1 in 400. In our case, 1 mbar out of nominal 1013 mbar meets this requirement. The instrument

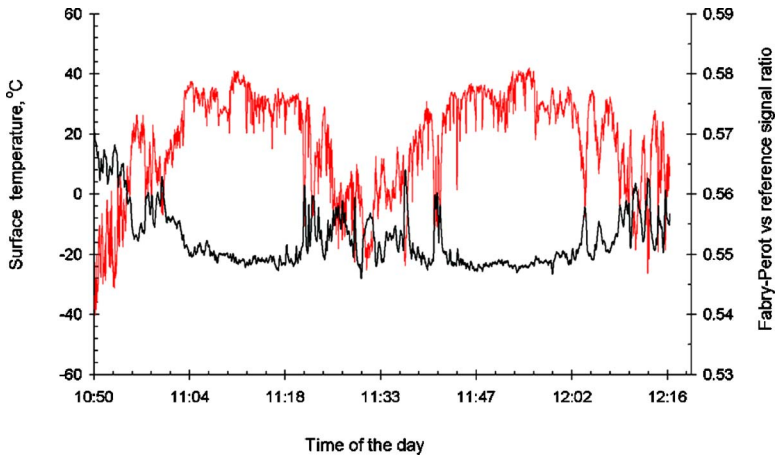

Fig. 11 Aircraft measurements of the ratio of Fabry-Perot to reference signal for the temperature-sensing channel (black line), and the surface temperature (gray), as functions of time. Data are taken at 1-s intervals with an instrument integration time of 0.1 s. Local daylight saving time is used.

also can be deployed on aircraft or satellites to perform space measurements. The detected sensitivity for the airborne experiments is 5 mbar. Reduced sensitivity for those measurements arises because atmospheric scattering makes the solar radiation path length more variable and uncertain.

The advantages of the presented technique are its sensitivity and ability to measure other trace gas species as well. The design is simple and cheap in comparison with other remote sensing instruments. The instrument's portability and its capability of real-time measurements are advantages also.

Acknowledgments

This research was sponsored by NASA's Earth Science Technology Office under grant NRA-01-OES-01.We acknowledge helpful discussions with S. Randolph Kawa, A. E. Andrews, and J. Burris of NASA Goddard Space Flight Center.

References

1. G. L. Stephens and A. Heidinger, "Molecular line absorption in a scattering atmosphere. Part I: theory," *J. Atmos. Sci.* **57**, 1599–1614 (1999).
2. G. L. Stephens and A. Heidinger, "Molecular line absorption in a scattering atmosphere. Part II: application to remote sensing in the O_2 A band," *J. Atmos. Sci.* **57**, 1615–1634 (1999).
3. G. L. Stephens and A. Heidinger, "Molecular line absorption in a scattering atmosphere. Part III: path length characteristics and effects of spatially heterogeneous clouds," *J. Atmos. Sci.* **59**(10), 1641–1654 (2001).
4. D. M. Stam, J. F. de Haan, J. W. Hovenier, I. Aben, and P. Stammes, "Detecting radiances in the O_2 A band using polarization-sensitive satellite instruments with application to the global ozone monitoring experiment," *J. Geophys. Res.* **105**(D17), 22379–22392 (2000).
5. H. Bovensmann, J. P. Burrows, M. Buchwitz, J. Frerick, S. Noël, V. V. Rozanov, K. V. Chance, and A. H. P. Goede, "SCIAMACHY: mission objectives and measurement modes," *J. Atmos. Sci.* **56**(2), 127–150 (1999).
6. R. Bennartz and J. Fischer, "A modified *k*-distribution approach applied to narrow band water vapor and oxygen absorption estimates in the near infrared," *J. Quant. Spectrosc. Radiat. Transf.* **66**(6), 539–553 (2000).
7. P. Dubuisson, R. Borde, D. Dessailly, and R. Santer, "In-flight spectral calibration of the oxygen A-band channel of MERIS," *Int. J. Remote Sens.* **24**(5), 1177–1182 (2003).
8. D. M. O'Brien, R. M. Mitchell, S. A. English, and G. A. Da Costa, "Airborne measurements of air mass from O_2 A-band absorption spectra," *J. Atmos. Ocean. Technol.* **15**, 1272–1286 (1998).
9. D. M. O'Brien and R. M. Mitchell, "Error-estimates for retrieval of cloud-top pressure using absorption in the A-band of oxygen," *J. Appl. Meteorol.* **31**(10), 1179–1192 (1992).
10. D. M. Stam, J. F. De Haan, and J. W. Hovenier, "Degree of linear polarization of light emerging from the cloudless atmosphere in the oxygen A band," *J. Geophys. Res.* **104**(D14), 16843–16858 (1999).
11. D. Wark and D. Mercer, "Absorption in the atmosphere by the oxygen A band," *Appl. Opt.* **4**, 839–844 (1965).
12. F. Saiedy, H. Jacobowitz, and D. Wark, "On cloud-top determination from Gemini-5," *J. Atmos. Sci.* **24**, 63–69 (1967).
13. A. Kuze and K. Chance, "Analysis of cloud-top height and cloud coverage from satellites using the O_2 A and B bands," *J. Geophys. Res.* **99**(D7), 14481–14491 (1994).
14. J. Fischer and H. Grassl, "Detection of cloud-top height from backscattered radiances within the oxygen A-band. Part 1: theoretical study," *J. Appl. Meteorol.* **30**, 1245–1259 (1991).
15. J. Fischer, W. Cordes, A. Schmitz-Pfeiffer, W. Renger, and P. Mörl, "Detection of cloud-top height from backscattered radiances within the oxygen A-band. Part 2: measurements," *J. Appl. Meteorol.* **30**(9), 1260–1267 (1991).
16. R. Boers, J. Spinhirne, and W. Hart, "Lidar observations of the fine-scale variability of marine stratocumulus clouds," *J. Appl. Meteorol.* **27**, 797–810 (1988).
17. F. Bréon and S. Bouffiés, "Land surface pressure estimate from measurements in the oxygen A absorption band," *J. Appl. Meteorol.* **35**, 69–77 (1996).
18. J. Daniel, S. Solomon, H. Miller, A. Langford, R. Portmann, and C. Eubank, "Retrieving cloud information from passive measurements of solar radiation absorbed by molecular oxygen and O_2-O_2," *J. Geophys. Res.* **18**(D16), 4515 (2003).
19. W. R. Skinner and P. B. Hays, "Brightness of the O_2 atmospheric bands in the daytime thermosphere," *Planet. Space Sci.* **33**(1), 17–22 (1985).
20. A. Bucholtz, W. R. Skinner, V. J. Abreu, and P. B. Hays, "The dayglow of the atmospheric band system," *Planet. Space Sci.* **34**(11), 1031–1035 (1986).
21. V. J. Abreu, A. Bucholtz, P. B. Hays, D. Ortland, W. R. Skinner, and J. H. Yee, "Absorption and emission line shapes in the O_2 atmospheric bands: theoretical model and limb viewing simulations," *Appl. Opt.* **28**(11), 2128–2137 (1989).
22. E. Georgieva, E. Wilson, M. Miodek, and W. S. Heaps, "Experimental data on CO_2 detection using Fabry-Perot-based optical setup for atmospheric observations," in *Optical Spectroscopic Techniques and Instrumentation for Atmospheric and Space Research V*, *Proc. SPIE* **5157**, 211–219 (2003).
23. W. S. Heaps, S. R. Kawa, and E. Georgieva, "Progression passive sensor for ultraprecise measurement of CO_2," in *Sixth International Symposium on Tropospheric Profiling: needs and technologies*, pp. 252–254 (2003).
24. J. Vaughan, *The Fabry-Perot Interferometer: History, Theory, Practice, and Applications*, A. Hilger, Bristol (1989).
25. G. Hernandez, *Fabry-Perot Interferometers*, Cambridge Univ. Press, New York (1986).
26. G. Slyusarev, *Aberration and Optical Design Theory*, Adam Hilger Ltd., Bristol (1984).
27. J. Mao and S. R. Kawa, "Sensitivity studies for space-based measurement of atmospheric total column carbon dioxide by reflected sunlight," *Appl. Opt.* **43**(4), 914–927 (2004).
28. S. R. Kawa, D. J. Erickson III, S. Pawson, and Z. Zhu, "Global CO_2 transport simulations using meteorological data from the NASA data assimilation system," *J. Geophys. Res.* **109**(D18312) (2004).
29. P. I. Palmer, D. J. Jacob, K. Chance, R. V. Martin, R. J. D. Spurr, T. Kurosu, I. Bey, R. Yantosca, A. Fiore, and Q. Li, "Air-mass factor formulation for differential optical absorption spectroscopy measurements from satellites and application to formaldehyde retrievals from GOME," *J. Geophys. Res., [Atmos.]* **106**(D13), 14539–14550 (2001).

Elena M. Georgieva is currently an associate research scientist at Goddard Earth Science and Technology Center, Universtiy of Maryland Baltimore County, and NASA's Goddard Space Flight Center. She received her PhD in physics in 1998 from the University of Sofia. She was a senior system scientist at Science Systems and Applications, Inc., and the Goddard Space Flight Center's Laser and Electro-Optics Branch working on instrument development for the measurement of atmospheric species. She was a research associate at the NIST Center for Neutron Research, Johns Hopkins University, and at the Physics Development at Georgetown University, where she worded on nanoparticles characterization and correlation spectroscopy. Her research interests are in remote sensing data analysis and validation, instrument development, spectroscopy, interferometry, and polarimetry. She has 24 refereed publications and is a number of Optical Society of America and SPIE—The International Society for Optical Engineering. She is currently with Goddard Earth Science and Technology Center, University of Maryland Baltimore County.

Emily Wilson joined the Laser and Electro-Optics Branch at NASA Goddard Space Flight Center as a physicist in 2005 following a postdoctoral position at the National Research Council from 2002–2005. Her research focuses on instrument development for measuring trace gases in the atmosphere. Her degrees include a PhD in chemistry from George Washington University, 2002, a MA degree in chemistry from Boston University, 1999, and a BS degree in chemistry from the University of Montana, 1995, where she was the recipient of the American Institute of Chemists Outstanding Chemistry Student Award in 1995. She has also worked as a science education assistant at the Lemelson Center for Invention and Inno-

vation at the National Museum of American History, Smithsonian Institution, producing science education programs for middle school students from 1997 to 1999.

M. Miodek: biography and photograph not available.

William S. Heaps has had a distinguished career in atmospheric science and remote sensing technology. With a BA degree in physics from Rice University and a PhD from University of Wisconsin, he joined NASA's Goddard Space Flight Center in 1977. His first effort was development of a balloon-borne laser-induced fluorescence instrument that succeeded in making some of the first measurements of stratospheric hydroxyl radical. In the 1980s he served on the mission planning group for the UARS satellite. At the same time he developed an airborne Raman lidar system to measure water vapor and methane, and aided in the development of the Solar Disk Sextant that made the most precise ever measurements of the diameter and shape of the Sun. In 1998, he left that Atmospheric Chemistry and Dynamics Branch to become branch head of the Laser and Electro-Optics Branch. While serving as branch head he became the Goddard principal investigator for NASA's Laser Risk Reduction Program to enhance performance and reliability of lasers for spaceborne remote sensing. He has participated in more than 15 balloon launches and has served as an airborne experimenter in a number of international measurement campaigns including TOTE/VOTE, SOLVE I, SOLVE II, PAVE, and INDEX-B operating lidars and Fabry-Pérot interferometers. Today he serves on the staff of the Instrument Systems and Technology Division as senior staff engineer for lasers and electro-optics.